A. WOŹNIAK[1], M. ADAMIAK[1*], G. CHLADEK[1], J. KASPERSKI[2]

THE INFLUENCE OF THE PROCESS PARAMETERS ON THE MICROSTRUCTURE
AND PROPERTIES SLM PROCESSED 316 L STAINLESS STEEL

Selective Laser Melting (SLM) is a modern manufacturing method with many applications in medicine, aerospace and automotive industries. SLM processed materials are characterized by good dimensional accuracy and properties comparable or superior to materials obtained by traditional processing methods. In this paper an SLM process was used to obtain 316L stainless steel parts. This paper presents the microstructure, chemical and phase composition, physicochemical and electrochemical properties of 12 groups of tested samples, differentiated by the SLM processing parameters. Based on the investigation, it can be inferred that the selection of the appropriate SLM parameters is very important to determined final material properties. The samples produced with the energy density $E = 600$ J/mm^3 were observed to possess optimum properties – a homogeneous structure, density closest to the desired one, good wettability and pitting corrosion resistance.

Keywords: SLM; 316L stainless steel; corrosion test; wettability

1. Introduction

Currently, there is a noticeable increase in the use modern manufacturing technologies based on CAD/CAM systems, such as three dimensional printing methods or additive manufacturing. The most popular Rapid Prototyping methods, which enable building parts from metallic powder are Selective Laser Sintering (SLS), Selective Laser Melting (SLM) and Direct Metal Laser Sintering (DMLS). In the latter method, the layer of output powder material, which is applied to the work platform with a blade, is a transition from the solid state to a liquid state and return (during rapid cooling) to the solid state [1-9]. In SLM processing, the selection of appropriate process parameters can be divided into four groups: (1) Sintered material – grain size, chemical composition, (2) Sintered parameters – scanning speed SP, laser output power P, laser beam diameter, point distance PD, (3) Sintered layer – layer thickness and (4) Economical factors – price of powder and totally price of process [8]. A very popular material used in SLM procedure is 316L stainless steel alloy. Most often, Cr-Ni-Mo containing austenitic steel like 316L is characterized by good corrosion resistance and mechanical properties. However, due to accelerated corrosion as a result of internal physiological environment and possible allergenic effects, Cr-Ni-Mo steel can be used only for short-term implants [10]. There are many publications on the parameters selection and properties of the 316L stainless steel components, obtained by SLM process [1-4], but the majority of research focuses on their mechanical properties and microstructure. This paper is focused on the physicochemical and electrochemical properties, which are very important for biomedical applications.

The aim of this work is to characterize 316L stainless steel components, manufactured by SLM to determine the effect of process parameters on their properties.

2. Materials and methods

The material used in this work, 316L stainless steel powder (Renishaw), with nominal chemical composition given in Table 1. The powder were spherical in shape with size fraction of 15 to 45 µm [11].

The samples were manufactured by Selective Laser Melting (SLM) using SLM/SLS machine type AM 125 (Renishaw, United Kingdom), equipped with a continuous wave Ytterbium

[1] SILESIAN UNIVERSITY OF TECHNOLOGY, FACULTY OF MECHANICAL ENGINEERING, DEPARTMENT OF ENGINEERING MATERIALS AND BIOMATERIALS, 18A KONARSKIEGO STR., 44-100, GLIWICE, POLAND
[2] MEDICAL UNIVERSITY OF SILESIA, SCHOOL OF MEDICINE WITH THE DIVISION OF DENTISTRY IN ZABRZE, DEPARTMENT OF PROSTHETIC DENTISTRY, PLAC AKADEMICKI 17, 41-902 BYTOM, POLAND

* Corresponding author: marcin.adamiak@polsl.pl
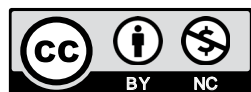
Chemical compositions of 316L stainless steel powder [14]

C	Si	Mn	P	S	Cr	Ni	Mo	O	N	Fe
≤0.03	≤1.00	≤2.00	≤0.045	≤0.03	16.00-18.00	10.00-14.00	2.00-3.00	≤0.01	≤0.10	Rest

fiber laser (YFL) with a wavelength of 1070 nm, power up to 200 W and a laser scanning speed up to 2000 mm/s and a laser beam diameter equals to 35 μm. The process was conducted under protective atmosphere of high purity argon [11].

As a part of this experiment an attempt was made to determine the influence of values of energy density (E) used in the SLM process on the properties of manufactured samples. The SLM process was carried out with an energy density calculated according to the formula $E = P/(t \times PD \times SP)$. The layer thickness ($t$) remained constant throughout the build process, while values of laser power (P), laser scanning speed (SP) and point distance (PD) were variable. The group of technological parameters of the SLM process and their values were presented in Table 2.

TABLE 2

The manufacturing parameters at different energy inputs

No.	Code	P, [W]	SP, [mm/s]	PD, [mm]	t, [mm]	E, [J/mm³]
1.	150/600/0.05/0.05	150	600	0.05	0.05	100
2.	150/400/0.05/0.05	150	400	0.05	0.05	150
3.	150/300/0.05/0.05	150	300	0.05	0.05	200
4.	150/300/0.02/0.05	150	500	0.02	0.05	300
5.	200/500/0.02/0.05	200	500	0.02	0.05	400
6.	150/300/0.02/0.05	150	300	0.02	0.05	500
7.	150/500/0.01/0.05	150	500	0.01	0.05	600
8.	200/300/0.02/0.05	200	300	0.02	0.05	680
9.	150/400/0.01/0.05	150	400	0.01	0.05	750
10.	200/500/0.01/0.05	200	500	0.01	0.05	800
11.	150/300/0.01/0.05	150	300	0.01	0.05	1000
12.	200/300/0.01/0.05	200	300	0.01	0.05	1333

The samples tested were in the form a cube with a side length of 10 mm. A meander scan strategy was employed for the production of the samples. The samples were built at 0° to the build direction. The scanning strategy and part orientation were designed with MARCAM AutoFab software (PresseBox, Germany). Residue and support structures were removed by hand to achieve a smooth final surface finish.

After SLM and finishing the samples were subjected to mechanical finishing, which consisted of two consecutive processes: mechanical grinding and mechanical polishing. First the samples were ground with MD – Piano disc (MD-Piano 200, 600 and 1200) then mechanical polishing was performed with diamond lapping compounds (PD-Paste 9 μm, 6 μm, 3 μm and 1 μm) and standard colloidal silica suspension – OP-U 0.04 μm. The grinding and polishing were carried out with the use of polishing-grinding machine TERGAMIN – 30 (Struers, Poland). In order to reveal surface morphological features, the samples were etched using a Nital solution (Ethanol 100 ml and Nitric acid 1-10 ml) [12].

2.1. Microscopic analysis

To visually inspect the surfaces of the samples, images were taken with an Axio observer Z1 (Zeiss, Germany).

2.2. SEM/EDS analysis

Scanning electron microscope Supra 35 (Zeiss, Germany) equipped with type SE detector for secondary electrons, was used for inspection of higher magnification images of surface topography. Microscopic inspection was carried out with an accelerating voltage of 20 kV. Additionally, the qualitative and quantitative of the chemical composition analyses were performed using energy dispersive X-ray spectroscopic (EDS) analysis. Five measurements were taken on randomly chosen areas for one group of samples.

2.3. XRD

Evaluation of phase composition of the tested samples was performed using X`Pert PRO X-ray diffractometer (Panalytical) equipped with a cobalt lamp x-ray source. The cobalt lamp was set to 40 kV and heater current of 30 mA was used. In order to perform the X-ray phase analysis in the Bragg-Brentano geometry the PICcel 3D detector was used. Measurements were made within the 2Θ Bragg angle range from 40 to 100°.

2.4. Density measurement

The density of the samples was determined by the buoyancy method based on Archimede`s principle [13]. The measurements were performed with the use a Radwag AS 220 R2 (Radwag, Poland) analytical balance with a precision of ±0.0001 g. Five measurements were made for each of the samples.

2.5. Surface roughness measurement

Surface roughness measurements were performed by the contact method with a Surtronic 25 surface roughness tester by Taylor Hobson (Poland). The measurements length was 0.8 mm and the measurements accuracy was ± 0.1 mm. Roughness parameter Ra – arithmetical mean roughness value determined the obtained results of measurements. Values of average of five measurements on each sample were given.

2.6. Wettability measurements and Surface Free Energy calculations

In order to determine the chemical character of tested materials, contact angle analysis was conducted. The sessile drop method was used to obtain the values of the contact angle. The measurements were carried on a Surftens Universal goniometer (OEG Company, Germany) and computer software to analyze the recorded drop image (Surften 4.5). Distilled water (POCH S.A.) and diiodomethane (Merck) were applied as measurements liquids, with drops 1.5 μm in volume, were placed on the surface of the tested samples. The study was carried out at room temperature $T = 23°C$ after the drop was placed measurements were taken after 20s. The duration of one measurement was 60 s. For the tested samples five measurements with the using the two liquids were performed and the average value was determined. The values for Surface Free Energy (SFE) and their polar and dispersion properties for the Owens – Wendt method [14] are given in Table 3. The SFE components were calculated based on average values of contact angle measurements.

TABLE 3

The values of SFE and their polar and apolar components for measure liquids used in Owens – Wendt method [14]

	Distilled water	Diiodomethane
γ_L, [mJ/m^2]	72.80	50.80
γ_L^d, [mJ/m^2]	21.80	0.00
γ_L^P, [mJ/m^2]	51.00	0.00

2.7. Pitting corrosion test

Pitting corrosion tests were performed by potentiodynamic method by recording the anodic polarization curve according to PE-EN ISO 10993-15 standard [15]. The test apparatus comprised of an Atlas 0531 EU potentiostat (ATLAS-SOLLICH, Poland), PC with AtlasLab software and electrochemical cell with a three-electrode system. A saturated Ag/AgCl electrode was used as a reference, the auxiliary electrode was a platinum wire (PTP-201) and the working electrode was r the sample to be tested. In the first step the open circuit potential E_{ocp} was determined and the measurements were started from the initial potential $E_{int} = E_{ocp} - 100$ mV. The potential value changed along the anodic direction and the applied scan rate was 1 mV/s. Once the maximum measuring range reached +2000 mV or anodic current density $i = 1$ mA/cm^2 the polarization direction was changed and return curves were recorded. Three samples from each test group were selected for testing. On this basis the characteristic parameters of corrosion were set: corrosion potential E_{corr} [mV], breakdowns potential E_{np} [mV], repassivation potential E_{cp} [mV]. The value of polarization resistance R_p [kΩ·cm^2] was determined by Tafel method. The tests were realized in Ringer's solution (NaCl – 8.6 g/l, KCl – 0.3 g/l, CaCl$_2$ 2H$_2$O – 0.33 g/l) at the temperature $T = 37 \pm 1°C$ and pH 6.9 ± 0.2.

2.8. Statistical analysis

In order to determine statistical significance of obtained measurements results between the study groups, statistical analysis was carried out with Statistica (Poland). The distributions of the residuals were tested with the Shapiro-Wilk test. Additionally, the equality of variances was tested with the use Levene test. Where the distribution of the residuals was normal and the variances were equal, the one-way ANOVA with Tukey HSD post host test were used. A value of $p < 0.05$ was considered to be statistically significant, while $0.05 < p < 0.10$ was considered to represent a non-significant

3. Results

3.1. Microscopic analysis

Figure 1 presents optical microscopic images of the surface morphology of the 316L stainless steel, obtained by SLM process. As can be observed, the microstructure of tested samples
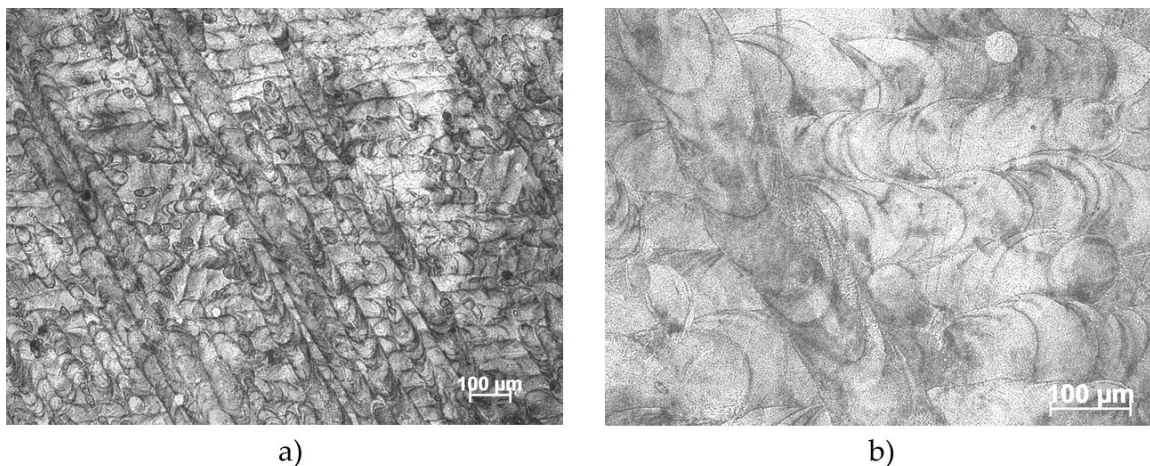

a)   b)

Fig. 1. Surface morphology of tested samples (7th group of samples) a) magnification × 25, b) magnification × 200

was typical of three dimensional printing processes (Fig. 1a). The samples were characterized by layered microstructure characterized by closely stacked scanning tracks. In the melt pool area, columnar grains are visible, which show growth in the direction of the thermal gradient through the melt pool boundaries. Based on the results of the authors' previous research [1,4] it has been stated that the similar relationship was obtained.

3.2. SEM/EDS analysis

Figure 2 presents examples results of microscopic observation of surface topography of samples 7th group, which were characterized by homogeneous structure free of defects. Based on local chemical analysis (Table 4) of this group of the samples, can be concluded, no significant deviations from the value of the material card are detected on the basis of the performed analysis (Table 1).

TABLE 4

Results of microchemical composition mean values and standard deviations

| Element	% weight	% atomic
Fe	65.5±1.2	65.2±0.8
Cr	18.5±0.9	19.7±0.3
Ni	12.6±0.9	12.0±0.5
Mo	2.6±0.2	1.5±0.1
Si	0.8±0.1	1.6±0.1

For the other samples group many defects, caused by the solidification process were observed. The most frequently observed defect was biding defect (Fig. 3a and b), which are cavities associated with the metallic spherical particles with the shape and size similar to the starting powder. Defects of this type are caused by incomplete melting of the powder as a result of low laser output energy during melting process. Another defect observed is balling, where agglomerates of ellipsoidal and spherical metallic balls form in order minimize surface free energy between them and molten tract. Pore formation due to gas entrapment (Fig. 3c) were also found to be typical structural defects.

The porosity, binding defects, gas pores and voids associated are the group of the most frequently identified defects, which is also indicated by other literature data [1-4]. In the case of biomedical materials, incomplete melting of powder at a local level and binding defects are damaging to the health – non melted powder grains can be distributed throughout the body with blood and body fluids. The final type of structural defect observed was layered voids (Fig. 3d), caused by rapid cooling, distinguished by crack formation along melt pool boundaries [1]. Based on the results of the authors' previous research [1,18] it has been stated that the similar relationship was obtained

3.3. XRD

The results of phase composition XRD spectra are shown in Figure 4. On the basis on the Schaeffler diagram [17] it can be concluded, that when the Cr_{eg}/Ni_{eg} ratio was less than 1.48, the powder grains solidified with the austenite being the primary or leading phase and the delta ferrite. In the present study, the obtained spectra show that the tested samples were characterized by the only presence of austenite phase with a preference for [111] plane orientation. Based on the local microchemical analysis, it can be concluded that the Cr/Ni ratio was approximately 1.47 – the low Cr/Ni ratio alloys only solidify within austenite mode at high cooling rates. The result of XRD analyzes obtained by Guo at al. [17] indicate that, the microstructure of 316L stainless steel obtained by bed fusion process may consisted of primary austenite and the delta ferrite. The fully austenitic microstructure obtained in the present study may be attributed to the higher cooling rates [17].
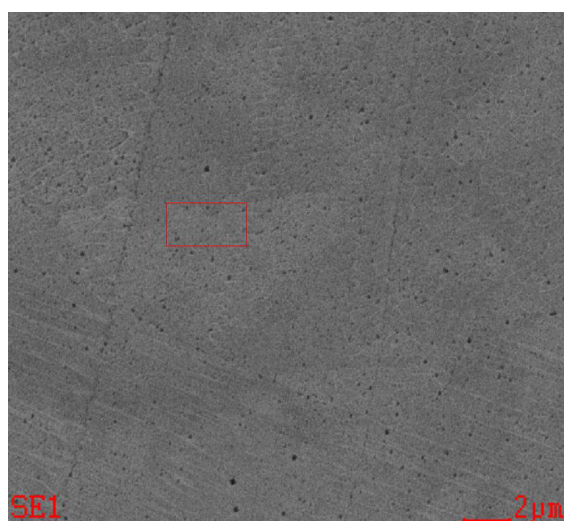
a)
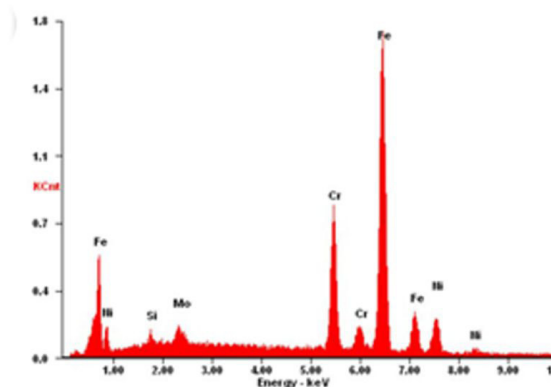
b)

Fig. 2. Examples results of SEM/EDS analysis of 7th samples group a) SEM image, b) Energy Dispersive spectroscopy (EDS) spectra
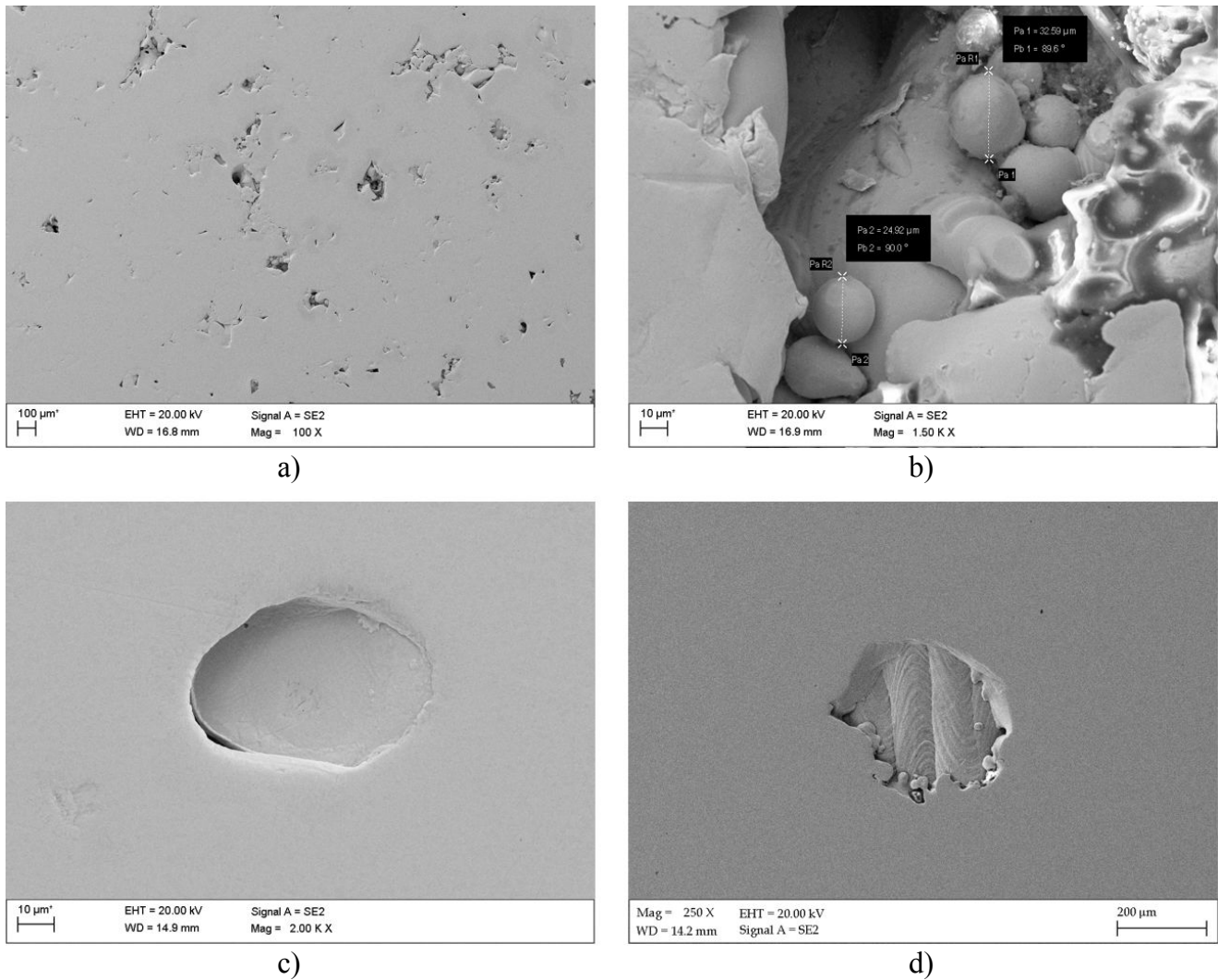
Fig. 3. Typical defects of melted materials a) binding defects, b) binding defects, c) gas pore, d) layered voids
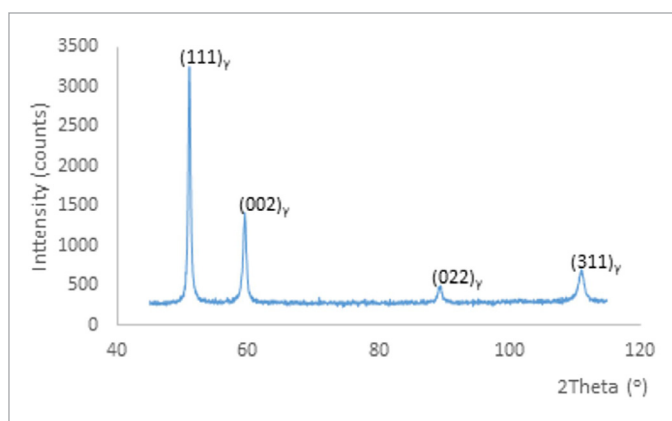

Fig. 4. X-ray diffraction pattern of 316L stainless steel

3.4. Density – Buoyancy method

The results of material density measurements are given in Table 5. The density of 316L stainless steel accordance to material manufacturer's data sheet (Renishaw) should be 7.99 g/cm^3.

The process parameters have a significant effect on the density of the tested samples ($p < 0.0001$). The values of densities of all tested samples were lower than desired density and were within the range of 7.00-7.81 g/cm^3. The 7th group samples (150/300/0.02/0.05), which were melted with the energy density $E = 600$ J/mm^3 are characterized by density close to 98% ($\rho = 7.81 \div 0.09$ g/cm^3), taking 7,99 g/cm^3 as the reference value, corresponding to 316L stainless steel. The values of material density characterized by $\rho_{rel} > 95$ % were obtained for 4th to 6th and 8th to 11th samples group. Based on the findings it can be concluded that the element characterized by high density can be produced with process parameter combination: high laser power in the range $150 \div 200$ W and low values of point distance (less than 0.02 mm). Similar dependence of material density increase along with the increase of laser power was obtained by Liverani et al [1]. The higher values of material density can be obtained as a result of changes in process parameter. Additionally, based on research conducted by Gao et al. [2] and Zhang et al. [15], it can be found that the SLM technology allow the manufacture of near full-density metallic components via fusion and re-solidification of fine elements.

TABLE 5

Results of tested samples density measurements – mean values and standard deviations. Groups with the same lowercase superscript letters for each column are not significantly different at the $p < 0.05$ level

Code	Energy Density E, [mJ/mm³]	Material Density
150/600/0.05/0.05	100	7.25 ± 0.09^{ab}
150/400/0.05/0.05	150	7.05 ± 0.12^{b}
150/300/0.05/0.05	200	7.00 ± 0.22^{b}
150/300/0.02/0.05	300	7.58 ± 0.16^{cde}
200/500/0.02/0.05	400	7.74 ± 0.08^{d}
150/300/0.02/0.05	500	7.72 ± 0.08^{d}
150/500/0.01/0.05	600	7.81 ± 0.09^{d}
200/300/0.02/0.05	680	7.75 ± 0.10^{d}
150/400/0.01/0.05	750	7.52 ± 0.18^{d}
200/500/0.01/0.05	800	7.60 ± 0.13^{d}
150/300/0.01/0.05	1000	7.74 ± 0.08^{d}
200/300/0.01/0.05	1333	7.39 ± 0.05^{ace}

3.5. Surface roughness measurements

The obtained results of surface roughness measurements indicate that the process parameters have a significant effect on the values of R_a parameter of the tested samples ($p < 0.0001$).

The lower value of R_a parameter was recorded for the 7th and 8th groups of the samples and the mean values were respectively $R_a = 3.8 \pm 0.1$ µm and $R_a = 3.9 \pm 0.1$ µm. In other tested samples, the values of surface roughness were higher. The highest values of R_a were observed for the samples sintered with the use of low values of energy density ($E = 100 \div 500$ mJ/mm³), and for the samples from groups 8th and above, the mean value of surface roughness were similar and were in the range $4.25 \div 5.35$ µm.

3.6. Wettability measurements and Surface Free Energy calculations

The obtained results of contact angle Θ measurements and surface free energy SFE calculated were given in Table 6. The process parameters have a significant effect on the values of contact angle of the tested samples ($p < 0.0001$). The highest value of contact angle was recorded for the 7th group of samples ($E = 600$ J/mm³) and the mean value was approximately 90° and amounted to $\Theta = 90 \pm 2.1°$, which indicate a low surface energy, hydrophobic character of the surface. The results of surface roughness and contact angle measurements indicate, that with together with decrease of the values of surface roughness parameter, the value of water-wetting angles increase [6,9]. It was observed that, when energy density used during SLM process is higher or lower than 600 J/mm³, lower values of contact angle were recorded for all tested samples. The contact angle values of less than 90° indicate the hydrophilic character of the surface. For all the tested samples, one can see a differences in values of Surface Free Energy SFE. The lowest value of SFE was recorded for the 7th group of samples and the mean value was $\gamma_S = 27.1$ mJ/m². For the other groups of tested samples the values of SFE were higher, and the highest value was obtained for the samples, produced with the low values of energy density (1st, 2nd, 3rd). Additionally, surface free energy calculated shows that for all tested samples except of the 2nd, 3rd and 4th groups, the high values of apolar components and low values of the polar ones were recorded. On this basis, it can be concluded that these surfaces exhibit a greater affinity to the apolar groups than to the polar ones.

3.7. Pitting corrosion test

The results of the potendiodynamic test in form anodic polarization curves were presented in Figure 5 and the character-

TABLE 6

Results of contact angle measurements and SFE calculated – mean values and for value for wetting angle results the standard deviations. Groups with the same lowercase superscript letters for each column are not significantly different at the $p < 0.05$ level

Code	Energy Density E, [J/mm³]	Measure liquid		Surface Free Energy, [mJ/m²]		
		Distilled water	Diiodomethane	γ_S	γ_d^S	γ_p^S
150/600/0.05/0.05	100	41.6 ± 8.9^{a}	43.1 ± 1.0	54.0	38.3	30.3
150/400/0.05/0.05	150	52.1 ± 4.3^{b}	41.1 ± 4.8	48.7	22.1	26.7
150/300/0.05/0.05	200	56.3 ± 11.2^{bc}	46.1 ± 3.7	45.8	21.8	24.0
150/300/0.02/0.05	300	52.2 ± 2.3^{b}	41.2 ± 4.1	45.9	22.2	23.8
200/500/0.02/0.05	400	61.4 ± 1.6^{bce}	44.3 ± 3.8	42.7	23.8	18.9
150/300/0.02/0.05	500	64.5 ± 1.2^{e}	45.6 ± 0.7	41.0	23.9	17.1
150/500/0.01/0.05	600	90.0 ± 2.1^{f}	62.5 ± 8.2	27.1	23.4	3.8
200/300/0.02/0.05	680	75.6 ± 3.7^{g}	51.2 ± 2.4	37.7	25.2	9.6
150/400/0.01/0.05	750	55.8 ± 5.3^{bc}	43.2 ± 1.1	46.0	23.8	21.7
200/500/0.01/0.05	800	66.7 ± 1.2^{eg}	46.1 ± 3.1	39.6	24.8	14.9
150/300/0.01/0.05	1000	64.0 ± 1.4^{ce}	51.5 ± 1.0	38.7	20.8	17.9
200/300/0.01/0.05	1333	64.6 ± 2.1^{ce}	51.4 ± 1.9	38.7	20.8	17.9

TABLE 7

Results of pitting corrosion test – mean values and standard deviations

Code	Energy density, $[J/mm^3]$	E_{corr}, [mV]	E_b, [mV]	E_{cp}, [mV]	R_p, $[\Omega/cm^2]$
150/600/0.05/0.05	100	−43±3	340±4	—	30±1
150/400/0.05/0.05	150	−137±3	321±2	−51±2	21±3
150/300/0.05/0.05	200	−124±2	365±3	—	24±2
150/300/0.02/0.05	300	−109±6	312±3	−43±3	39±1
200/500/0.02/0.05	400	−184±3	530±3	—	18±3
150/300/0.02/0.05	500	−177±5	504±3	−36±2	14±3
150/500/0.01/0.05	600	−133±5	561±4	+15±2	27±3
200/300/0.02/0.05	680	−172±3	—	—	16±2
150/400/0.01/0.05	750	−174±3	492±2	+3±1	20±2
200/500/0.01/0.05	800	−173±3	302±3	—	25±3
150/300/0.01/0.05	1000	−186±3	580±3	—	19±2
200/300/0.01/0.05	1333	−170±2	204±3	—	22±3

istic values describing the pitting corrosion resistance are shown in Table 7. For all tested samples, the polarization curves were similar in character – the hysteresis loop were recorded and the obtained polarization curves shown the presence of breakdown potential E_b. However, not for the all samples the existence of repassivation E_{cp} potential has been stated. The highest value of breakdown potential was recorded for 11th group of the tested samples and the mean value was $E_b = 580 \pm 3$ mV. The values of the corrosion potential E_{corr} for all the tested samples were in the range −186 mV ÷ −42 mV, and the highest values were recorded for the samples from 1st group. Additionally, it was stated that values of polarization potential R_p for tested samples were in the range from 16 Ω/cm^2 for the samples form 8th group to 39 Ω/cm^2 for the samples 4th group. Based on the obtained results, it can be concluded that the samples 7th group were characterized by optimal pitting corrosion resistance – the mean values of pitting corrosion was $E_{corr} = −133 \pm 5$ mV, which is the average value among those registered. Additionally, for this group of the samples high values of breakdown potential $E_b = 560 \pm 4$ mV and repassivation potential $E_{cp} = 15 \pm 2$ were recorded. Additionally based on the obtained results and the literature date, it can be consulted that the lower values of surface roughness

parameter affect the improvement of the corrosion resistance of the material. In orthopedic applications, the Cr-Ni-Mo stainless steel can be used only for short-term implant. For this reason, it is important that the final implant is characterized by a low surface roughness. Significant development of surface topography favors osteoinduction processes, and thus hinders reoperation.

4. Conclusion

Bed fusion technology does not appear to exhibit limitations from a design point of view – it's possible to manufacture very complex geometries and assemblies possessing high dimensional accuracy (creation of geometrical shapes that cannot be manufactured by other means) [9]. However, this is not case from a technological perspective. The properties of manufactured details depend on the process parameter. The result of performed experimental prove that selection of the right SLM parameters is very important in determining the final properties, which enable safe use of created elements and their reliability. Based on obtained results and literature data [1-9], it can be concluded that important parameters, which have significant influence on properties of melted samples is laser power output, laser scanning speed and point distance. These process parameters make it difficult to obtain 100 % density in the obtained during SLM process elements. The 7th group samples (150/300/0.02/0.05), which were melted with the energy density $E = 600$ J/mm³ are characterized by optimal results, which do not constitute the prescribed values. For 7th samples group the mean value of density was close to 98 % ($\rho = 7.81 \div 0.09$ g/cm³), taking 7,99 g/cm³ as the reference value, corresponding to 316L stainless steel. The phase structure investigations show that the samples 7th group had a homogeneous and defects free full γ austenite microstructure, which was related to the chemical composition of the material. The surface topography of these samples groups was defect free. Additionally, for 7th samples group the lowest
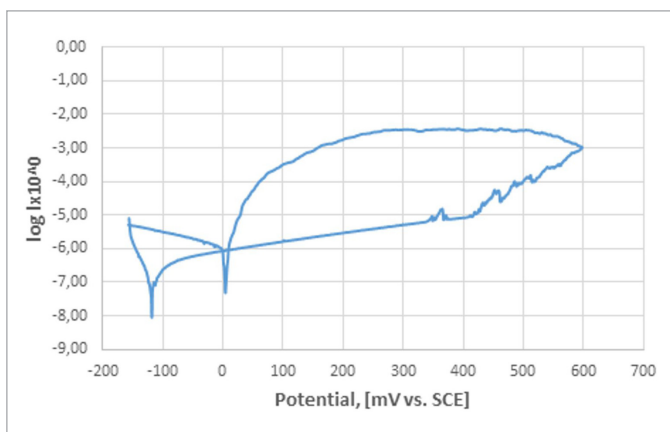

Fig. 5. Example polarization curves for 7th group of the tested samples

value of surface roughness $R_a = 3.8 \pm 0.1$ and the highest value of contact angle $\Theta = 90 \pm 2.1^\circ$ were recorded. The other groups of tested samples were characterized by low density and surface topography with definitely more surface defects.

REFERENCES

[1] E. Liverani, S. Toschi, L. Ceschini, A. Fortuanto, J. Mater. Process. Technol. **249**, 255-263 (2017).

[2] P. Gao, B. Zuo, Ch. Hugan, H. Gao, J. Mater. Process. Technol. **240**, 12-22 (2017).

[3] J.A. Cherry, H.M Davies, S. Mehmood, N.P. Lavery, S.G.R. Brown, J. Sienz, Int. J. Adv. Manuf. Technol. **76**, 869-879 (2015).

[4] W. Gao, Y. Zhang, D. Ramanujan, K. Ramani, Y. Chen, Ch.B. Williams, Ch.C.L. Wang, Y.C. Sinh, S. Zhang, P.D. Zavatteri, Comput. Aided Des. **69**, 65-89 (2015).

[5] B. Zhang, H. Liao, Ch. Coddet, Appl. Surf. Sci. **279**, 310-316 (2013).

[6] A. Ziębowicz, A. Woźniak, B. Ziębowicz, The Influence of Technology on the Physicochemical and Electrochemical Properties of the Prosthetic Materials in: Gzik M., Tkacz E., Paszenda Z., Piętka E. (eds), Innovations in Biomedical Engineering. IBE 2017. Advances in Intelligent Systems and Computing, Vol. 623. Springer, Cham (2017).

[7] M. Król, L.A. Dobrzański, Ł. Reimann, I. Czaja, Arch. Mater. Sci. Eng. **60** (2), 87-92 (2013).

[8] A. Stwora, G. Skrabalak, J. Achiev. Mater. Manuf. Eng. **61** (2), 375-380 (2013).

[9] A. Ziębowicz, A. Woźniak, B. Ziębowicz, M. Adamiak, P. Boryło, Arch. Mater. Sci. Eng. **89** (1), 20-26 (2018).

[10] W. Kajzer, A. Kajzer, W. Walke, J. Marciniak, J. Achiev. Mater. Manuf. Eng. **18** (1-2), 115-118 (2006).

[11] http://www.renishaw.com

[12] R. Cheraghali, Sh. Mordadi, M. Ghoranneviss, A.P. Aberomand, S.A. Kohrrmi, Asian J. Chem. **23** (7), 2833-2836 (2011).

[13] B. Adriaan, M. Spiergings, R. Eggenberger, Rapid Prototyping J. **17** (5), 380-386 (2011).

[14] S. Firlik, J. Molenda, Chemik **64** (4), 238-245 (2010).

[15] PN-EN ISO 10993-13:2010.

[16] B. Zhang, L. Dembinski, C. Coddet, Mat. Sci. Eng. **584**, 21-31 (2013).

[17] K. Zhang, S. Wang, H. Shang, Mater. & Design **55**, 104-119 (2014).